ACS Catalysis

pubs.acs.org/acscatalysis Research Article

Bioinspired Atomic Manganese Site Accelerates Oxo-Dehydrogenation of N-Heterocycles over a Conjugated Tri-*s*-Triazine Framework

Zhou Zhang,[†] Wengang Liu,*[,†] Yuanyuan Zhang, Jingwen Bai, and Jian Liu*

Cite This: *ACS Catal.* 2021, 11, 313–322 Read Online

ACCESS | Metrics & More | Article Recommendations | Supporting Information

ABSTRACT: Herein, taking inspirations from metalloenzymes, we constructed atomically dispersed manganese sites anchored onto conjugated tri-*s*-triazine units of graphitic carbon nitride as a bioinspired photocatalyst (Mn_1/tri-CN) for the oxo-dehydrogenation of N-heterocycles. The primary coordination sphere of atomic Mn-N_2 sites (role i: oxygen activation) as well as the $\pi-\pi$ stacking interactions between tri-*s*-triazine units and substrate mimicking the secondary coordination sphere (role ii: substrate adsorption) synergistically realized high-efficiency electron transfer/utilization in photocatalytic oxidation reactions, as was demonstrated experimentally and theoretically. The Mn_1/tri-CN catalyst exhibited impressive oxo-dehydrogenation activity and selectivity toward a broad scope of N-heterocycles in an air atmosphere. The current work suggests that simultaneously engineering the metal active sites of catalysts and the adaptive local environment of the matrix may open an avenue for the synthesis of fine chemicals.

KEYWORDS: *bioinspired catalyst, photocatalysis, active sites, synergistic catalysis, conjugated polymer*

Downloaded via AUCKLAND UNIV OF TECHNOLOGY on December 19, 2020 at 16:03:58 (UTC).
See https://pubs.acs.org/sharingguidelines for options on how to legitimately share published articles.

INTRODUCTION

In Nature, metalloenzymes catalyze a number of bond-making and bond-breaking redox reactions involving the transfer of multiple electrons and protons.[1−5] In order to accomplish numerous redox reactions, the limited active metal sites (one or a few) as well as the second-sphere interactions in the protein matrix are both critical. When it comes to the activation of oxygen in Nature, biochemical reactions involving oxygen can smoothly occur on [Fe] of cytochrome *c*, [Cu] of laccase and Mn_4CaO_x clusters of the oxygen-evolving complex of photosystem II under ambient conditions, while the noncovalent structural recognition (including hydrogen bonding, van der Waals interactions, and hydrophobic effects) in the secondary sphere facilitates the transfer of electrons and protons.[6] Bioinspired catalysts with metalloenzyme-like catalytic sites may open an avenue for the efficient synthesis of high-value chemicals, especially under solar light illumination.

In the past, researchers used atomically dispersed metal active sites with a porphyrin-like structure (M-N-C, M = Co, Fe, Ni, Cu, etc.) to mimic biological metalloenzymes as superior photo-/electrocatalysts (more details are given in Scheme S1).[7−11] Certainly, these M-N-C single-atom catalysts are more amenable to the rational design of active sites, which provide a good platform for constructing the structure−activity relationship between the active sites and reaction performance.[12−14] There have been enormous efforts toward the modulation of metal sites, including the metal atom type and coordination numbers.[7,15−17] However, as demonstrated in enzymatic catalysis, the metal active sites along with the secondary coordination sphere of the matrix synergistically determine the overall catalytic performance,[18] which has rarely been reported in previous investigations of heterogeneous photocatalysts.

With metalloenzymes as the inspiration, integrating the biomimetic atomic metal sites into conjugated polymer supports with an adaptive local environment will be promising for the efficient synthesis of fine chemicals. Considering the structural characteristics of aromatic N-heterocycles, we deliberately chose graphitic carbon nitride with tri-*s*-triazine units (tri-CN) as a support, which could bring interactions with N-heterocycles via $\pi-\pi$ stacking interactions. The atomically dispersed Mn sites were anchored onto tri-*s*-triazine units, which act to activate oxygen for the oxo-dehydrogenation probe reaction of aromatic N-heterocycles.[19−23] A wide

Received: October 26, 2020
Revised: December 9, 2020

© XXXX American Chemical Society

https://dx.doi.org/10.1021/acscatal.0c04651
ACS Catal. 2021, 11, 313−322

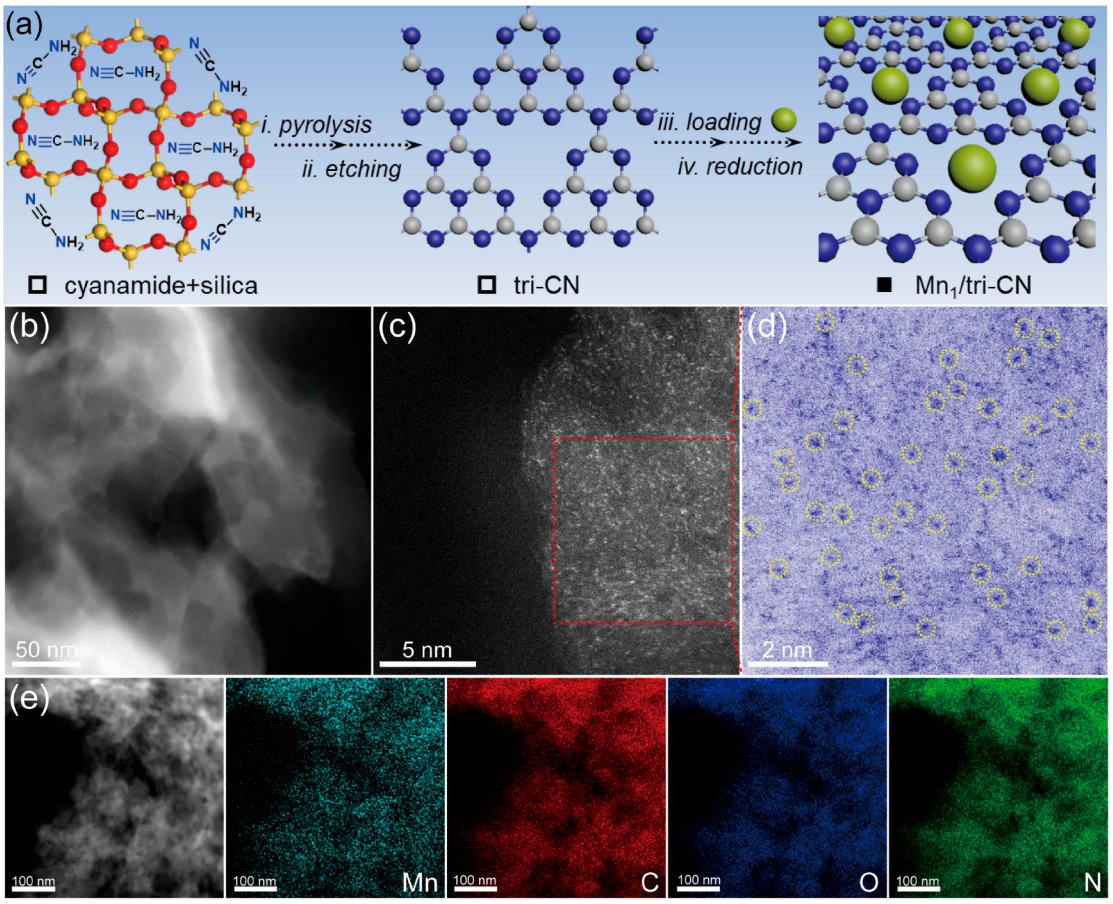

Figure 1. Structure characterization of Mn_1/tri-CN photocatalyst. (a) Schematic preparation of the Mn_1/tri-CN photocatalyst. STEM image (b) and atomic resolution HAADF-STEM images (c, d) of the Mn_1/tri-CN sample. (e) Corresponding EDS mapping of Mn, C, O, and N elements, respectively.

scope of substrates such as 1,2,3,4-tetrahydroquinolines (THQs), tetrahydroisoquinolines (iso-THQs), and various functionalized derivatives can be smoothly oxidized into the corresponding products with up to 99% selectivity. Mechanistic studies prove that the atomic Mn sites in Mn_1/tri-CN catalysts could rapidly activate O_2 molecules to generate superoxide radical anions ($O_2^{\bullet-}$) as highly reactive oxygen species. The atomic Mn-N_2 dopants realize fast kinetics for O_2 activation via accelerating excited electron transfer and electron utilization in photocatalysis. Meanwhile, tri-*s*-triazine units of the support close to the Mn-N_2 sites mediate the adsorption behavior of an analogous tetrahydroquinoline molecule via $\pi-\pi$ stacking interactions.[24] Consequently, Mn_1/tri-CN realizes efficient utilization of excited electrons and superior performance for photocatalytic oxo-dehydrogenation.

RESULTS AND DISCUSSION

Catalyst Preparation and Structural Characterization. Mn_1/tri-CN was synthesized by successive polymerization−impregnation−activation procedures, as illustrated in Figure 1a (more synthesis details can be found in the Experimental Section). The as-prepared Mn_1/tri-CN sample shows a typical 2D layered stacking morphology according to scanning electron microscopy (SEM, Figure S1). No Mn nanoparticles or tiny clusters of the Mn_1/tri-CN sample are observed in transmission electron microscopy (TEM) images (Figure S2) and high-resolution scanning transmission electron microscopy (STEM) images (Figure 1b and Figure S3). No diffraction peaks corresponding to Mn species were detected from X-ray diffraction patterns (XRD), and only one broad diffraction peak at 27° of the tri-CN reference and Mn_1/tri-CN sample assigned to the (002) planes of carbon nitride was observed (Figure S4).[25,26] These characterization results indicated that the Mn species of Mn_1/tri-CN sample must be highly dispersed as single atoms or sub-nanoclusters. ICP analysis revealed that the Mn loading was 4.5 wt %.

To obtain the atomic phase of Mn species in Mn_1/tri-CN sample, aberration-corrected high-angle annular dark field scanning transmission electron microscopy (HAADF-STEM) was performed. The isolated bright dots in Figure 1c,d and Figure S5 can be assigned to the single Mn atoms according to the sensitive *Z* contrast between the heavy element and light elements (Mn vs C/N/O), confirming the atomic dispersion of Mn species in the as-prepared Mn_1/tri-CN sample. Furthermore, the electron energy loss spectroscopy (EELS) atomic spectra of the Mn_1/tri-CN sample clearly confirmed the coexistence of Mn and N elements, indicating that single Mn atoms should be bonded with neighboring N atoms in the Mn_1/tri-CN catalyst (Figure S6). In addition, the uniform dispersion of Mn, C, O, and N elements was also depicted by energy dispersive spectroscopy (EDS) elemental mapping (Figure 1e). On the basis of the Mn loading and Brunauer−Emmett−Teller (BET) surface area (Figures S7 and S8 and Table S1), the density of single Mn atoms in the Mn_1/tri-CN sample can be roughly estimated as 3.15 Mn atoms/nm^2. To

https://dx.doi.org/10.1021/acscatal.0c04651
ACS Catal. 2021, 11, 313−322

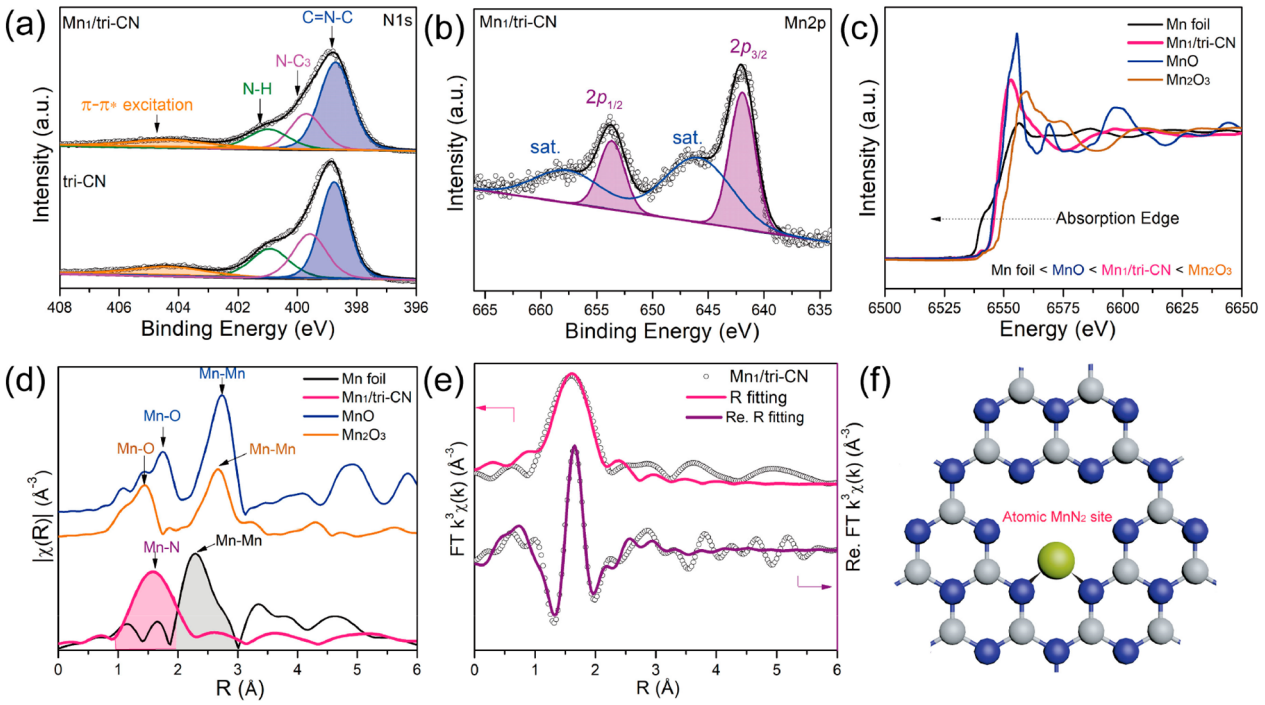

Figure 2. Chemical state and coordination information for the Mn_1/tri-CN photocatalyst and reference sample. High-resolution N 1s (a) and Mn 2p (b) XPS of the Mn_1/tri-CN sample. (c) Normalized Mn K-edge XANES spectra of the Mn_1/tri-CN sample and standard references. (d) Fourier-transformed k^2-weighted EXAFS spectra of different samples. (e) Mn K-edge *R* space EXAFS fitting results of the Mn_1/tri-CN sample. (f) Schematic model of the atomic Mn-N_2 site obtained from EXAFS fitting results.

the best of the authors' knowledge, this Mn site density of the Mn_1/tri-CN sample is 1 order of magnitude higher than that of most of the reported M-N-C single-atom catalysts,[7,27,28] ensuring the existence of abundant sites for potential catalysis reactions.

Chemical State and Coordination Environment of Catalysts. The XPS survey spectra confirmed the existence of Mn, C, O, and N components in the Mn_1/tri-CN sample and tri-CN reference (Figure S9). In addition, the atomic percentage of the N element was dominant on the basis of a surface composition analysis (Table S2). In high-resolution N 1s XPS spectra of the Mn_1/tri-CN sample and tri-CN reference, four fitted peaks were located at 398.8, 399.5, 401, and 404.3 eV (Figure 2a), which can be assigned to the pyridinic N in tri-*s*-triazine units, graphitic N, N−H species, and a $\pi-\pi^*$ excitation transition typical for conjugated aromatic rings, respectively.[29,30] The relative concentrations of different N species are shown in Table S3. Among them, high-content pyridinic N is generally considered as the coordinating ligands for transition metals.[8,31,32] Notably, the introduction of atomic Mn dopants did not change the π-electron conjugation ofthe semiconductor matrix since there was no dramatic variation in the location or intensity of $\pi-\pi^*$ excitation peaks. Similar results can also be found in C 1s spectra (Figure S10). The oxidation state of the Mn species was determined as divalent Mn^{II} according to binding energies of 641.9 eV ($2p_{3/2}$) and 653.6 eV ($2p_{1/2}$) in the Mn 2p XPS spectra (Figure 2b).[1,33] This assignment was further verified by a subsequent X-ray absorption spectroscopy (XAFS) analysis.

The local environment of Mn sites in the Mn_1/tri-CN sample was then determined by XAFS characterizations. From the X-ray absorption near-edge structure (XANES) spectra in Figure 2c and Figure S11, we observed that the adsorption edge of the Mn_1/tri-CN sample moved toward higher energy in comparison to Mn foil and was located between the $Mn^{II}O$ and $Mn^{III}_2O_3$ references. In combination with Mn 2p XPS results, the valence state of Mn atoms in the Mn_1/tri-CN sample was confirmed as divalent cations (Mn^{2+}) with higher binding energy owing to the chemical bonding between Mn centers and the surrounding ligands. In order to clarify the bonding environment of Mn^{2+} cations, extended X-ray fine structure (EXAFS) spectra were analyzed. Fourier-transformed (FT) EXAFS spectra for the Mn_1/tri-CN sample and standard references are shown in Figure 2d. The scattering oscillation of the EXAFS spectrum for the Mn_1/tri-CN sample was quite distinct from other references, demonstrating the chemical environment of Mn atoms in the Mn_1/tri-CN sample was different from those in metallic manganese and manganese oxide (e.g., MnO and Mn_2O_3), respectively. The first coordination shell with a peak at 1.6 Å for the Mn_1/tri-CN sample can be attributed to the coordination between Mn atoms and light N/C elements. For comparison, metallic Mn−Mn bonds were located at 2.3 Å in the Mn foil. These EXAFS results further proved that the Mn atoms were atomically dispersed in the Mn_1/tri-CN sample. To unravel the local structure of atomic Mn sites in the Mn_1/tri-CN sample, least-squares EXAFS fitting was performed.[34] The best-fitting EXAFS curve in *R* and *k* space is shown in Figure 2e and Figures S12 and S13, and the corresponding extracted fitting parameters are summarized in Table S4. The coordination number of Mn−N_x bonding in the first coordination sphere was estimated to be 2 (Table S4), where the fitted *R*-space curves including the FT real part of Mn-N_2 models could well reproduce the experimental curves of the Mn_1/tri-CN sample (Figure 2e). On the basis of the EXAFS fitting results, the geometric structure of atomic Mn sites in the Mn_1/tri-CN sample was proposed as the Mn-N_2 model, as illustrated in Figure 2f. In this model, single Mn atoms are coordinated by

https://dx.doi.org/10.1021/acscatal.0c04651
ACS Catal. 2021, 11, 313−322

two pyridinic N atoms in a triazine-rich graphitic carbon nitride matrix.

Photocatalytic Oxo-Dehydrogenation of N-heterocycles. The obtained Mn_1/tri-CN sample was then applied to photocatalytic oxidation reactions under visible light irradiation. As a probe reaction, photocatalytic oxo-dehydrogenation of N-heterocycles to produce high-value quinoline compounds was carried out at 25 °C in an air atmosphere. A digital photo of the detailed experimental setup for this photocatalytic reaction system is included in Figure S14. Remarkably, this oxo-dehydrogenation reaction conducted on the Mn_1/tri-CN sample achieved the highest reactivity with up to 99% quinoline selectivity, and the selectivity of undesired **2b** (3,4-dihydroquinoline) byproduct was negligible (entry 1, Table 1).

Table 1. Screen of Photocatalysts for Oxo-Dehydrogenation of 1,2,3,4-Tetrahydroquinoline under Different Conditions[a]

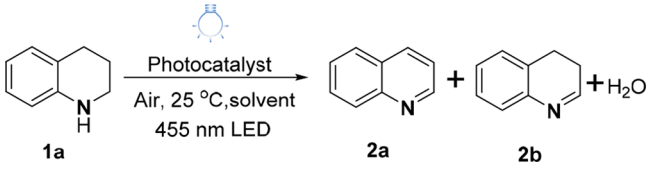

1a 2a 2b

				selectivity[c] (%)	
entry	catalyst	solvent	conversion[c] (%)	2a	2b
1	Mn_1/tri-CN	MeCN	99	99	<1
2	none	MeCN	N.D.		
3[b]	Mn_1/tri-CN	MeCN	N.D.		
4	bulk CN	MeCN	13	99	<1
5	tri-CN	MeCN	61	99	<1
6	Mn/tri-CN	MeCN	60	99	<1
7	Fe_1/tri-CN	MeCN	35	76	24
8	Co_1/tri-CN	MeCN	62	99	<1
9	Ni_1/tri-CN	MeCN	33	72	28
10	Mn_1/tri-CN	MeOH	7	99	<1
11	Mn_1/tri-CN	ethanol	40	37	63
12	Mn_1/tri-CN	i-PrOH	80	42	58

[a]Reaction conditions unless specified otherwise: 16 mmol % catalyst, 0.1 mmol substrates, 20 mL solvent, blue LED (455 nm), 25 °C, air atmosphere. Reaction time: 8 h. [b]Without light illumination. [c]The conversion and selectivity were determined by GC-MS analysis. N.D.: not detected.

As expected, no activity toward quinoline formation was observed without a photocatalyst or light irradiation (entries 2 and 3, Table 1). In contrast, the bulk carbon nitride (bulk CN) showed poor activity, while the tri-CN semiconductor and Mn/tri-CN nanoparticle catalyst with high metal loading gave a moderate conversion (entries 4–6, Table 1). Interestingly, inferior performance was obtained by using other metal M_1/tri-CN samples as photocatalysts (M = Co/Fe/Ni) under identical conditions, indicating the superiority of atomic Mn sites (entries 7–9, Table 1). In addition, solvent screening experiments demonstrated that the activity of the Mn_1/tri-CN sample was significantly affected by solvent type and acetonitrile may be the optimal solvent in this photocatalytic reaction (entries 10–12, Table 1).

To validate the catalytic generality of the Mn_1/tri-CN catalyst in photocatalytic oxo-dehydrogenation, the scope of other N-heterocycles was also tested under optimal conditions (Table S5). All of the N-heterocycle substrates can be smoothly converted into the corresponding desired products with high selectivity. For example, the oxo-dehydrogenation of an iso-THQ substrate was rapidly completed within only 2 h (entry 2, Table S5). Substrates with electron-deficient substituents (e.g., nitro, bromo) and electron-rich groups (e.g., methyl, hydroxy, methoxy) were also well tolerated. Moreover, reactions of sterically hindered substrates, such as 2-methyl-1,2,3,4-tetrahydroquinoline, resulted in 92% conversion and 99% selectivity within 24 h (entry 5, Table S5). Moreover, important pharmaceutical chemicals including indoline and tetrahydroquinoxaline gave a high conversion of 82–99% with a desired product yield of 94–99% (entries 9–10, Table S5). It is also noted that high temperature, high oxygen pressure, and noble-metal catalysts are often required to finish the oxo-dehydrogenation of N-heterocycles in traditional organic transformation.[35,36] Our Mn_1/tri-CN photocatalyst exhibited superior activity and selectivity under mild conditions (room temperature, air atmosphere, acceptorless dehydrogenation).

Following the catalytic activity tests of the Mn_1/tri-CN catalyst, the catalytic stability and recyclability of catalyst were also investigated, which are crucial for heterogeneous catalysts.[37] For each recycle test, the recycled catalyst was separated by simple centrifugation and washing. The Mn_1/tri-CN catalyst was continuously used for at least four cycles without any decay in activity and selectivity (Figure 3a). From the XRD pattern (Figure 3b) and FT-IR spectra (Figure 3c), we did not observe any change in crystal phase or composition of the spent Mn_1/tri-CN catalyst. In addition, the high-resolution Mn 2p (Figure 3d) and N 1s (Figure S15) XPS spectra of the used catalyst showed peak profiles similar to those of the fresh catalyst except for a slightly decreasing change in intensity. As shown in Figure S16, the HAADF-STEM images showed that the Mn species of the spent Mn_1/tri-CN catalyst still retained single-atom dispersion without any aggregation. In combination with catalyst recycle tests and other characterizations including XPS, FT-IR, and XRD, we concluded that the Mn_1/tri-CN photocatalyst had robust stability in such oxo-dehydrogenation reactions of N-heterocycles.

Roles of Atomic Mn Dopants in Enhancing Photocatalytic Performance. The optical properties of the Mn_1/tri-CN catalyst were investigated in order to elucidate the roles of atomic Mn dopants in enhancing photocatalytic oxidation performance. A diffuse reflectance UV–vis test showed the light absorption threshold of Mn_1/tri-CN catalyst underwent a red shift in comparison to the pristine tri-CN semiconductor (Figure S17a). The enhanced optical response in the visible light region facilitated the electron photoexcitation of semiconductors under the reaction conditions (455 nm). The estimated band gap energies of the Mn_1/tri-CN catalyst and tri-CN reference derived from Tauc plots were 2.62 and 2.78 eV, respectively (Figure S17b). As a result of atomic Mn dopants, the Mn_1/tri-CN catalyst with a narrow band gap for the enhanced absorption of visible light was obtained. Moreover, photoluminescence spectra (PL) showed that the Mn_1/tri-CN catalyst had a drastic decrease in emission intensity in comparison to the pristine tri-CN catalyst (Figure S18), suggesting the lower recombination of photoexcited electron–hole (e^--h^+) pairs. Thus, we deduced that atomic Mn dopants may serve as electron acceptors, where the photoexcited electrons on the conduction band of tri-CN semiconductors can be trapped by the atomic Mn sites and the

https://dx.doi.org/10.1021/acscatal.0c04651
ACS Catal. 2021, 11, 313–322

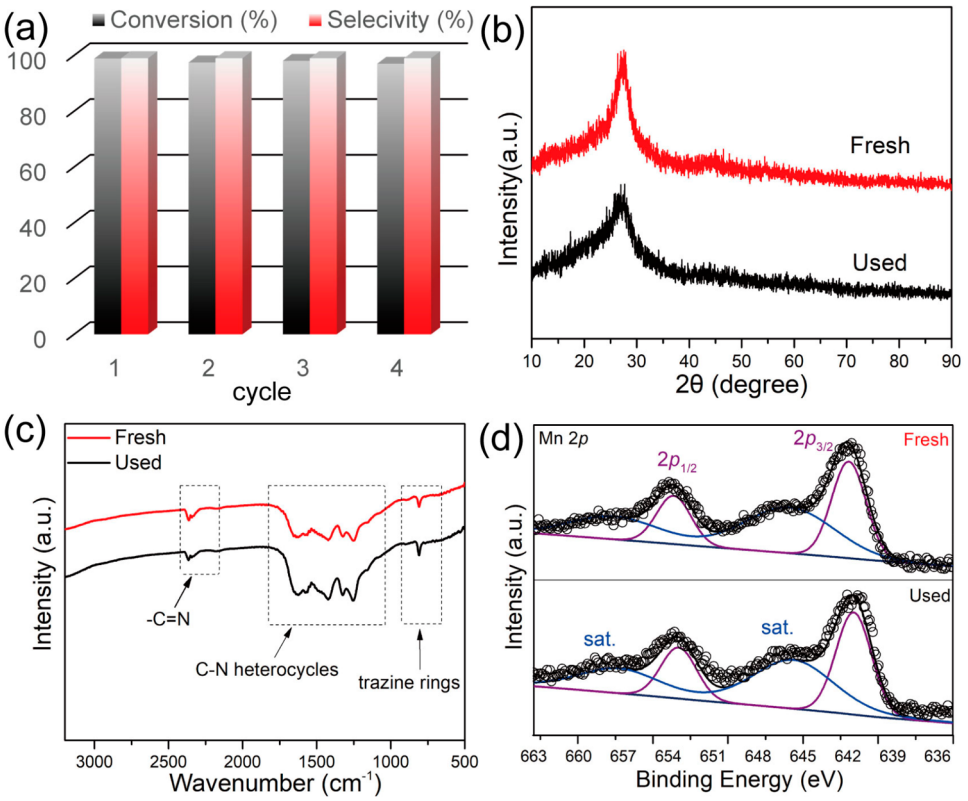

Figure 3. Investigation of catalytic recyclability and stability of the Mn_1/tri-CN photocatalyst. (a) Recycling stability of Mn_1/tri-CN for oxo-dehydrogenation of THQs. (b) XRD pattern, (c) FT-IR spectra, and (d) Mn 2p XPS spectra of the fresh and spent Mn_1/tri-CN catalysts.

efficient separation of e^--h^+ pairs leads to higher apparent activity.

To further verify the efficient separation efficiency of e^--h^+ pairs in the Mn_1/tri-CN catalyst, photocurrent response tests and electrochemical impedance spectroscopy (EIS) were also performed. The photocurrent in Figure S19 is generated by the separation and diffusion of photogenerated e^--h^+ pairs in semiconductors. The enhanced photocurrent of the Mn_1/tri-CN catalyst was attributed to the improved charge mobility. Similar results can also be found in the EIS plots. In EIS Nyquist plots, the radius of a high-frequency semicircular arc corresponds to the charge transfer resistance (R_{ct}) at the contact interface between the electrolyte solution and the electrode.[38] As shown in Figure S20, the arc radius of EIS plots corresponding to the Mn_1/tri-CN catalyst was much smaller than that of tri-CN catalyst, indicating the better conductivity and higher electron mobility rate of the Mn_1/tri-CN catalyst.[39] Therefore, the Mn_1/tri-CN catalyst has great advantages in efficient photogenerated e^--h^+ separation and fast interfacial transfer.

Adsorption Behaviors of Reactive Molecules on Active Sites. The origin of photocatalytic performance boosted by atomic Mn dopants is not simply attributed to integrating the sensitive optical response with robust photo-generated e^--h^+ pairs; the adsorption behaviors of reactive molecules including the substrate and O_2 onto the genuine active sites in the Mn_1/tri-CN catalyst should also be considered. Thanks to the well-defined structure of the single-atom catalyst, the geometric structure of atomic Mn sites in Mn_1/tri-CN catalyst had been identified as Mn-N_2 sites. Thus, we used density functional theory (DFT) calculations to establish Mn-N_2 sites into the conjugated tri-*s*-triazine framework as an adsorption surface. Here, the adsorption energy (ΔE_{ads}) of an adsorbate molecule (iso-THQ and O_2) was calculated by the following equation (Figure 4a): $\Delta E_{ads} = E_{surf\text{-}mol*} - E_{surf} - E_{mol}$.[30] Interestingly, we found that the tri-*s*-triazine units of such conjugated supports can interact with N-heterocycles (iso-THQs) via $\pi-\pi$ stacking interactions. According to the aforementioned N 1s XPS, the Mn_1/tri-CN catalyst has good conjugation structures with enriched π-electrons. Thereby, the analogous iso-THQs molecules with aromatic rings can be adsorbed onto the π-rich triazine units via the $\pi-\pi$ conjugation effect.[40,41] Moreover, we carefully investigated the $\pi-\pi$ stacking interactions for iso-THQ molecules adsorbing on different binding sites of the conjugated tri-*s*-triazine surface (Figure S21). Among them, the calculated ΔE_{ads} value of −0.93 eV for the iso-THQ substrate onto the tri-*s*-triazine unit (site 1.3) is the lowest value (Figure 4b). In other words, the tri-*s*-triazine unit close to the Mn-N_2 sites was the most thermodynamically stable adsorption site for the iso-THQ substrate absorbing onto the surface of the Mn_1/tri-CN catalyst. On the other hand, oxygen molecules can be strongly adsorbed on the atomic Mn-N_2 sites via an end-on adsorption configuration, where the ΔE_{ads} value was as low as −3.03 eV (site 2, Figure 4b). Such a strong interaction between oxygen and Mn-N_2 sites activated oxygen molecules and caused an increase in the length of the O═O bond from 1.226 to 1.298 Å (Figure 4c). The adsorbed O_2 molecules with enlarged bond length can be regarded as highly reactive oxygen species. Therefore, DFT calculations showed that there were synergistic effects of the Mn_1/tri-CN catalyst in photocatalytic oxo-dehydrogenation of N-heterocycles. Specifically, tri-*s*-triazine units (site 1) of semiconductors control the adsorption of the N-heterocycle substrate via $\pi-\pi$ stacking

https://dx.doi.org/10.1021/acscatal.0c04651
ACS Catal. 2021, 11, 313−322

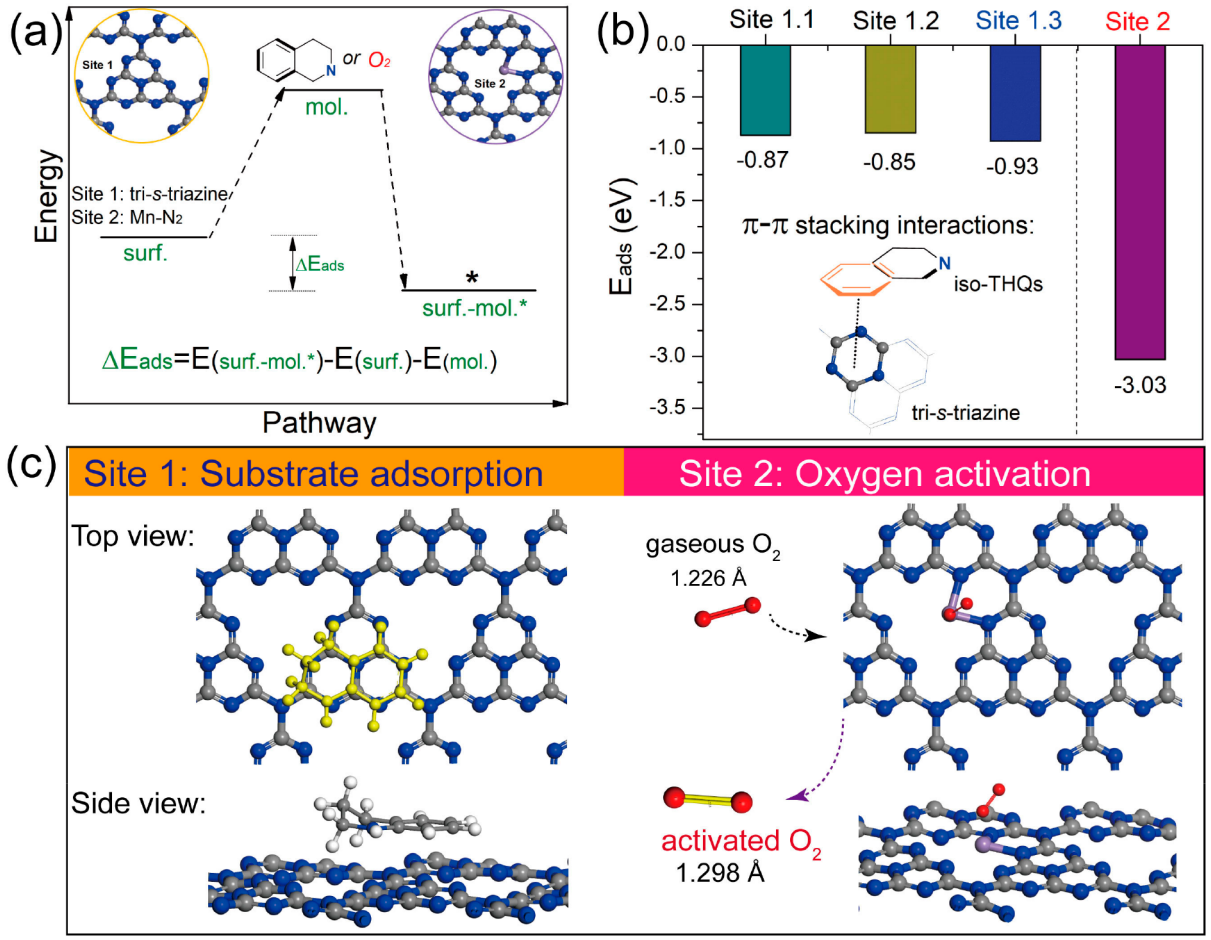

Figure 4. Theoretical calculations for the adsorption and activation of reactants on the Mn_1/tri-CN photocatalyst. (a) DFT calculation for the adsorption energy (ΔE_{ads}) of an iso-THQ substrate and O_2 molecule onto the surface of the Mn_1/tri-CN catalyst. (b) Calculated ΔE_{ads} values of adsorbate molecules on different binding sites. (c) Schematic adsorption configuration of adsorbate molecules on dual active sites.

interactions and meanwhile the atomic Mn-N_2 sites (site 2) are responsible for the adsorption and activation of oxygen molecules (Figure 4c).

Proposed Synergistic Catalysis Mechanism for Photocatalytic Oxo-Dehydrogenation. To gain more insight into the reaction mechanism, control experiments and electron paramagnetic resonance (EPR) measurements were carried out. Under optimal reaction conditions, the ubiquitous air was selected as the oxidant for the photocatalytic dehydrogenation reaction, indicating the benign environmental tolerance of this reaction system. It is worth mentioning that a high conversion of 1,2,3,4-tetrahydroquinoline can also obtained under a pure oxygen atmosphere. However, by switching the reaction atmosphere to an inert gas, such as argon or carbon dioxide, the Mn_1/tri-CN catalyst exhibited negligible reactivity (Figure 5a). Thus, the reaction pathway involving oxygen is dominant in such a photocatalytic reaction. EPR experiments with using 5,5-dimethyl-1-pyrroline *N*-oxide (DMPO) as a radical spin trapping agent was used to unravel the genuine reactive oxygen species.[42] As a blank experiment, no free radical signals were observed from EPR under dark conditions (Figure S22). Under visible light irradiation, the strong characteristic peaks of DMPO-$O_2^{\bullet-}$ superoxide radical anions with an ideal 1:1:1:1 quartet EPR signal was clearly detected for the Mn_1/tri-CN catalyst (Figure 5b).[43,44] For comparison, the intensity of $O_2^{\bullet-}$ generated by the Mn_1/tri-CN catalyst is much higher than that of the tri-CN catalyst. Moreover, reactive species quenching experiments were also performed to verify the contribution of $O_2^{\bullet-}$ radicals and other free radicals such as hydroxyl radicals (OH) and singlet oxygen ($^1O_2$) to this reaction (Figure S23). When the $^{\bullet}$OH scavenger TBA (*tert*-butanol) was added to the reaction system, the yield of quinoline product was almost unchanged, indicating that $^{\bullet}$OH hardly participates in the reaction. When TRP (L-tryptophan) was chosen as the $^1O_2$ scavenger, the yield of quinoline product decreased from 99% to 68%, indicating the trace generation of singlet $^1O_2$. Notably, the addition of the $O_2^{\bullet-}$ scavenger pBQ (*p*-benzoquinone) resulted in a severe degradation in the target yield from 99% to 26%. Therefore, the superoxide radical anions should be the dominant reactive species in the photocatalytic oxo-dehydrogenation of N-heterocycles. In combination with DFT results that O_2 molecules were activated by atomic Mn-N_2 sites, we suggest that the high-density atomic Mn-N_2 active sites can rapidly activate oxygen to highly reactive oxygen species ($O_2^{\bullet-}$).

On the basis of the above experimental and theoretical results, a plausible synergistic catalysis mechanism for photocatalytic oxidative dehydrogenation of THQ in the Mn_1/tri-CN catalyst system is proposed.[21] As shown in Figure 5c, by mimicking the primary and secondary coordination sphere of metalloenzyme, atomic Mn-N_2 sites and conjugated tri-*s*-triazine units in Mn_1/tri-CN catalyst collaborated to

https://dx.doi.org/10.1021/acscatal.0c04651
ACS Catal. 2021, 11, 313−322

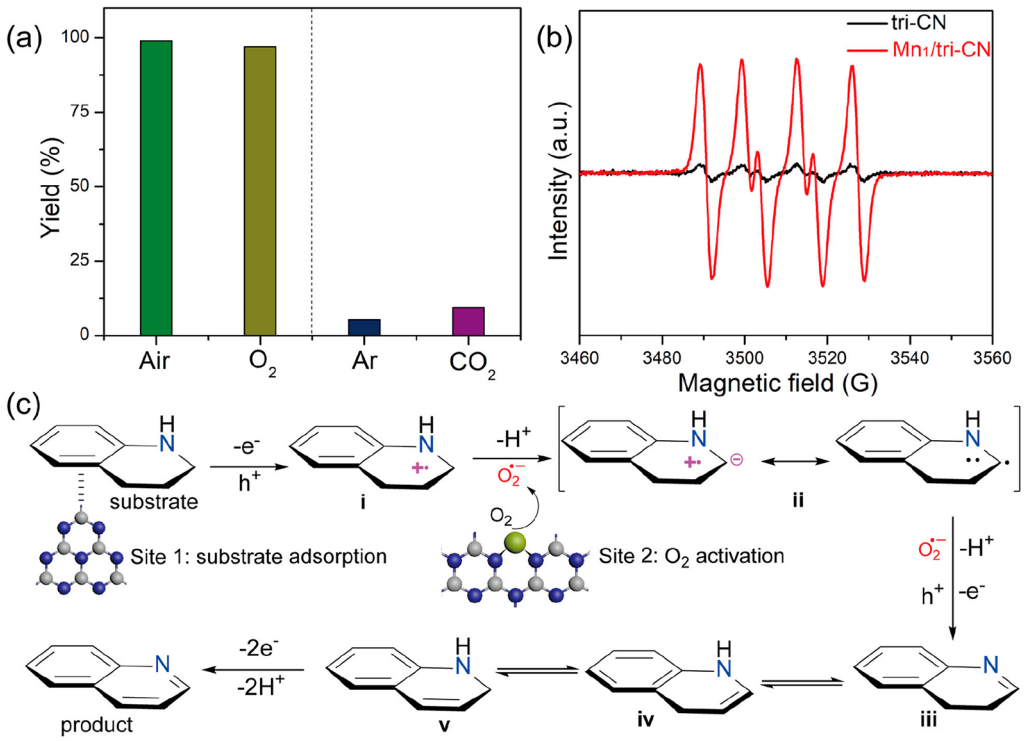

Figure 5. Proposed synergistic catalysis mechanism for photocatalytic oxo-dehydrogenation. (a) Oxo-dehydrogenation of 1,2,3,4-tetrahydroquinoline (THQ) over Mn_1/tri-CN under different atmospheres. (b) EPR spectrum of an aqueous solution of Mn_1/tri-CN and tri-CN (10 mg/mL) with DMPO (0.44 M). (c) Proposed mechanism for the photocatalytic oxo-dehydrogenation of 1,2,3,4-tetrahydroquinoline by Mn_1/tri-CN under visible light irradiation.

accomplish such a photocatalytic oxo-dehydrogenation reaction. First, photogenerated e^--h^+ pairs were generated on the tri-CN semiconductors. Meanwhile, the substrate was adsorbed by tri-*s*-triazine units of the tri-CN support via $\pi-\pi$ stacking interactions. Then, the photogenerated holes capture one electron of an N atom in THQ to yield intermediate **i**. Subsequently, $O_2^{\bullet-}$ radical activated Mn-N_2 sites abstract the α-H of intermediate **i** to form intermediate **ii**. Next, intermediate **iii** (3,4-dihydroquinoline) is obtained from intermediate **ii** by releasing one proton (H^+) and one electron (e^-). Then, 3,4-dihydroquinoline undergoes an isomerization reaction to generate intermediates **iv** and **v**. The final product was formed by removing an additional two H^+ and two e^- from intermediate **v**.

CONCLUSION

In summary, we successfully integrated the atomic Mn−N_2 sites into conjugated polymer as bioinspired Mn_1/tri-CN for photocatalytic oxidative dehydrogenation of N-heterocycles. It exhibits excellent photocatalytic activity, high selectivity, robust stability and wide substrate scope under mild conditions (e.g., visible-light, room temperature and raw air atmosphere). Experimental and theoretical analysis indicated that the excellent performance of Mn_1/tri-CN catalysts was attributed to synergistic catalysis mechanism involving atomic Mn−N_2 sites and conjugated tri-*s*-triazine units. Specifically, the atomic Mn−N_2 sites realize fast kinetics for O_2 activation, while tri-*s*-triazine units of support control the substrate adsorption via $\pi-\pi$ stacking interactions. This study reveals that bioinspired heterogeneous catalysts with well-defined active sites and noncovalent interaction may open an avenue for precise synthesis in organic transformation.

EXPERIMENTAL SECTION

Chemicals and Materials. All of the reagents and solvents were used as commercially available without further purification. Manganous acetate ($C_4H_6MnO_4$, 98%) was purchased from Energy Chemical Reagent Corp. Cyanamide solution (50 wt %), 5,5-dimethly-1-proline *N*-oxide (DMPO), and cyanamide were purchased from Sigma-Aldrich LLC. 1,2,3,4-Tetrahydroquinoline and other conventional reagents were purchased from Aladdin Bio-Chem Technology Co. Ltd.

Catalyst Preparation. Tri-*s*-triazine-rich carbon nitride (tri-CN) was prepared from cyanamide (NH_2CN) following a thermal polymerization process using silica gel as a template. Specifically, 2 g of a cyanamide solution and 750 mg of silica gel were mixed in an aqueous solution and subsequently dried in a rotary evaporator. The obtained powder was then placed in a quartz boat with a cover and pyrolyzed at 550 °C under N_2 for 4 h. The tri-CN product was obtained through an etching treatment in 10 wt % HF solution for 12 h to remove the template.

Mn_1/tri-CN was synthesized via a facile postloading method. A typical preparation of the Mn_1/tri-CN photocatalyst was as follows: 300 mg of tri-CN and 43.4 mg of manganous acetate were dissolved in 50 mL of 1 wt % acetic acid/methanol solution. The mixture was stirred for 1 h, followed by drying in a rotary evaporator. The obtained powder was heated in a tube furnace at 300 °C under a 5% H_2/95% Ar atmosphere with a heating ramp of 5 °C/min. The temperature was kept at 300 °C for 1 h. The final product was denoted as the Mn_1/tri-CN catalyst. As a comparison, Fe_1/tri-CN, Co_1/tri-CN, and Ni_1/tri-CN were synthesized through a similar preparation procedure except for different metal precursors. The Mn clusters supported on graphitic carbon nitride (denoted as

https://dx.doi.org/10.1021/acscatal.0c04651
ACS Catal. 2021, 11, 313−322

Mn/tri-CN) were synthesized through a similar preparation procedure except for a different magnesium precursor loading (Mn 10 wt %).

Characterizations. The as-obtained products were characterized by X-ray diffraction (XRD) patterns on a Rigaku D/MAX2500PC X-ray diffractometer with Cu Kα (λ= 1.5406 Å) radiation at a voltage of 40 kV and 150 mA. XRD patterns were scanned over the angular range of 10−90° (2θ) with a step size of 0.02°. The metal loadings of samples were determined with inductively coupled plasma atomic emission spectroscopy (ICP-AES). The transmission electron microscopy (TEM) images were measured with a JEOL Model JEM 2010 EX instrument at an accelerating voltage of 200 kV. HAADF-STEM characterization was conducted on a JEOL JEM-ARM200F instrument . X-ray photoelectron spectroscopy (XPS) measurements were performed on a Thermo ESCALAB XI$^+$ spectrometer. Electron paramagnetic resonance (EPR) measurements were carried out a with Bruker Model A300 spectrometer.

Data Collection and Analysis for XAS Spectra. Mn K-edge X-ray absorption spectra were acquired at room temperature in fluorescence mode at the National Synchrotron Radiation Research Center (NSRRC) using a Si (311) double-crystal monochromator. The energy was calibrated using Mn foil. The XAFS raw data were background-subtracted, normalized, and Fourier-transformed by the standard procedures with the Athena program (version 0.9.25). A least-squares curve fitting analysis of the EXAFS $\chi(k)$ data was carried out using the Artemis program (version 0.9.25) with the theoretical scattering amplitudes, phase shifts, and the photoelectron mean free path for all paths calculated by the ab initio code FEFF8. The details of fitting parameters are discussed in Table S4 in the Supporting Information.

Catalytic Reactions. The light-induced oxo-dehydrogenation reactions were carried out in a quartz tube irradiated with a photocatalytic reaction device (China Education Au-light Company, CEL-PCRD300-12, 25 W). Under standard conditions, the photocatalyst and 1,2,3,4-tetrahydroquinoline (12.54 μL, 0.1 mmol) were dispersed in the reaction medium (20 mL) in a quartz reactor. The reaction suspension was connected with an atmosphere of air and stirred at room temperature, and then the reaction was started under LED light irradiation (455 nm). After the reaction, the suspension was filtered through a porous membrane and the filtrate was analyzed by GC-MS (Shimadzu QP2010 SE).

Reactive Species Quenching Experiments and EPR Trapping Tests. Under the optimal reaction conditions, radical quenching experiments were performed through the addition of different radical scavengers. Specifically, 5 mM TRP (L-tryptophan) was chosen as the singlet oxygen ($^1O_2$) scavenger, 5 mM TBA (*tert*-butanol) was chosen as the hydroxyl radical ($^\bullet$OH) scavenger, and 5 mM pBQ (*p*-benzoquinone) was chosen as the superoxide radical ($O_2^{\bullet-}$) scavenger, respectively. For the EPR trapping test, 5,5-dimethyl-1-proline *N*-oxide (DMPO) was used as the superoxide radical ($O_2^{\bullet-}$) trapping reagent. A 4 mg portion of tri-CN or Mn_1/tri-CN catalyst was dispersed into 2 mL of methanol, forming a 2 mg/mL homogeneous suspension, and then 50 μL of a methanol solution of DMPO was added to the above suspension. After that, EPR signals were collected with a Bruker Model A300 spectrometer under visible light irradiation (λ > 400 nm) or in the dark.

Photoelectrochemical Tests. Photoelectrochemical tests were conducted with a three-electrode system on a CHI 660 electrochemical workstation, using a Pt wire as the counter electrode and an Ag/AgCl electrode as the reference electrode. The working electrode was prepared with fluorine−tin oxide (FTO) glass. A 5 mg sample was dispersed in 1 mL of ethanol by sonication to form a slurry. The slurry was dropped on FTO glass with an active area of 1 cm^2. The working electrode was dried in air at 60 °C and further dried at 120 °C for 2 h to improve adhesion.

DFT Calculations. All of the first-principles calculations of the study were performed using Dmol^3. The exchange and correlation terms were determined using the generalized gradient approximation (GGA) in the form proposed by Perdew, Burke, and Ernzerhof (PBE). For all elements, the all-electron method was applied (the basis set as DNP with the file is 4.4). Brillouin zone integration was performed using a 6 × 6 × 1 Monkhorst−Pack grid for a periodic slab with one single-layer planar substrate sheet and a 24 Å vacuum between the sheet and its periodic images. The cutoff was set as 4.5 Å, and a 0.005 Ha smearing was used to facilitate the self-consistent field (SCF) convergence. The thresholds of energy, force, and displacement are 10^{-5} hartree, 2×10^{-3} hartree/atom for the maximum force, and 5×10^{-3} Å for displacement.

The perfect conjugated tri-*s*-triazine framework consists of one layer and was constructed in a periodic simulation lattice built with three dimensions of x = 29.5 Å, y = 14.7 Å, and z = 10 Å. Subsequently, the Mn-N_2 structure was obtained by doping Mn atoms in the conjugated tri-*s*-triazine framework system. Then types of optimized interaction patterns (top and side views are shown in Figure S21 in the Supporting Information) and adsorption energies of adsorbate molecules (tetrahydroisoquinoline or O_2) adsorbed on the conjugated tri-*s*-triazine framework surface were designed and calculated.

The adsorption energy of an adsorbate molecule (tetrahydroisoquinoline or O_2) on the substrate surface (ΔE_{ads}) was calculated by eq 1

$$\Delta E_{ads} = E_{surf\text{-}mol*} - E_{surf} - E_{mol} \quad (1)$$

where E_{surf} and E_{mol} represent the energies of the substrate surface and the adsorbate molecule, respectively. $E_{surf\text{-}mol*}$ is the total energy of one of the adsorption configurations. A negative value of E_{ads} indicates that the process is an exothermic reaction, and high negative value corresponds to a stronger interaction, which indicates more heat release and a more stable product.

■ ASSOCIATED CONTENT

Supporting Information

The Supporting Information is available free of charge at https://pubs.acs.org/doi/10.1021/acscatal.0c04651.

Experimental section including the SEM, TEM, STEM, XRD, HAADF-STEM results, nitrogen adsorption−desorption isotherms, XPS survey spectra of the Mn_1/tri-CN catalyst and the tri-CN control sample, and additional tables to support the results (PDF)

■ AUTHOR INFORMATION

Corresponding Authors

Wengang Liu − *College of Material Science and Engineering, Qingdao University of Science and Technology, Qingdao*

https://dx.doi.org/10.1021/acscatal.0c04651
ACS Catal. 2021, 11, 313−322

266042, People's Republic of China; Email: liuwengang@qust.edu.cn

Jian Liu − *College of Material Science and Engineering, Qingdao University of Science and Technology, Qingdao 266042, People's Republic of China*; orcid.org/0000-0002-9684-339X; Email: liujian@qust.edu.cn

Authors

Zhou Zhang − *College of Material Science and Engineering, Qingdao University of Science and Technology, Qingdao 266042, People's Republic of China*

Yuanyuan Zhang − *College of Material Science and Engineering, Qingdao University of Science and Technology, Qingdao 266042, People's Republic of China*

Jingwen Bai − *College of Material Science and Engineering, Qingdao University of Science and Technology, Qingdao 266042, People's Republic of China*

Complete contact information is available at: https://pubs.acs.org/10.1021/acscatal.0c04651

Author Contributions

†W.L. and Z.Z. contributed equally to this work.

Notes

The authors declare no competing financial interest.

■ ACKNOWLEDGMENTS

The authors are grateful for the support from the National Natural Science Foundation of China (21902082, 21802080), the Natural Science Foundation of Shandong Province (ZR2019JQ05), the Key Basic Research Project of the Natural Science Foundation of Shandong Province (ZR2019ZD47), the Education Department of Shandong Province (2019KJC006), and the Original Innovation Project of Qingdao City (19-6-2-72-cg).

■ REFERENCES

(1) Yang, Y.; Mao, K.; Gao, S.; Huang, H.; Xia, G.; Lin, Z.; Jiang, P.; Wang, C.; Wang, H.; Chen, Q. O-, N-Atoms-Coordinated Mn Cofactors within a Graphene Framework as Bioinspired Oxygen Reduction Reaction Electrocatalysts. *Adv. Mater.* **2018**, *30* (28), 1801732.

(2) Pan, H. J.; Huang, G.; Wodrich, M. D.; Tirani, F. F.; Ataka, K.; Shima, S.; Hu, X. A Catalytically Active [Mn]-Hydrogenase Incorporating a Non-Native Metal Cofactor. *Nat. Chem.* **2019**, *11*, 669−675.

(3) Ghosh, T.; Maayan, G. Efficient Homogeneous Electrocatalytic Water Oxidation by a Manganese Cluster with an Overpotential of Only 74 mV. *Angew. Chem., Int. Ed.* **2019**, *58* (9), 2785−2790.

(4) Zhang, R.; Qin, Y.; Zhang, L.; Luo, S. Mechanistic Studies on Bioinspired Aerobic C-H Oxidation of Amines with an ortho-Quinone Catalyst. *J. Org. Chem.* **2019**, *84* (5), 2542−2555.

(5) Yuan, H.; Yoo, W. J.; Miyamura, H.; Kobayashi, S. Discovery of a Metalloenzyme-like Cooperative Catalytic System of Metal Nanoclusters and Catechol Derivatives for the Aerobic Oxidation of Amines. *J. Am. Chem. Soc.* **2012**, *134* (34), 13970−13973.

(6) Le, J. M.; Bren, K. L. Engineered Enzymes and Bioinspired Catalysts for Energy Conversion. *ACS Energy Lett.* **2019**, *4* (9), 2168−2180.

(7) Liu, W.; Zhang, L.; Liu, X.; Liu, X.; Yang, X.; Miao, S.; Wang, W.; Wang, A.; Zhang, T. Discriminating Catalytically Active FeN_x Species of Atomically Dispersed Fe-N-C Catalyst for Selective Oxidation of the C-H Bond. *J. Am. Chem. Soc.* **2017**, *139* (31), 10790−10798.

(8) Liu, W.; Chen, Y.; Qi, H.; Zhang, L.; Yan, W.; Liu, X.; Yang, X.; Miao, S.; Wang, W.; Liu, C.; Wang, A.; Li, J.; Zhang, T. A Durable Nickel Single-Atom Catalyst for Hydrogenation Reactions and Cellulose Valorization under Harsh Conditions. *Angew. Chem., Int. Ed.* **2018**, *57* (24), 7071−7075.

(9) Yang, H. B.; Hung, S.-F.; Liu, S.; Yuan, K.; Miao, S.; Zhang, L.; Huang, X.; Wang, H.-Y.; Cai, W.; Chen, R.; Gao, J.; Yang, X.; Chen, W.; Huang, Y.; Chen, H. M.; Li, C. M.; Zhang, T.; Liu, B. Atomically Dispersed Ni(I) as the Active Site for Electrochemical CO_2 Reduction. *Nat. Energy* **2018**, *3* (2), 140−147.

(10) Tian, S.; Wang, Z.; Gong, W.; Chen, W.; Feng, Q.; Xu, Q.; Chen, C.; Chen, C.; Peng, Q.; Gu, L.; Zhao, H.; Hu, P.; Wang, D.; Li, Y. Temperature-Controlled Selectivity of Hydrogenation and Hydrodeoxygenation in the Conversion of Biomass Molecule by the Ru_1/mpg-C_3N_4 Catalyst. *J. Am. Chem. Soc.* **2018**, *140* (36), 11161−11164.

(11) Zhang, L.; Wang, A.; Wang, W.; Huang, Y.; Liu, X.; Miao, S.; Liu, J.; Zhang, T. Co-N-C Catalyst for C-C Coupling Reactions: On the Catalytic Performance and Active Sites. *ACS Catal.* **2015**, *5* (11), 6563−6572.

(12) Wang, A.; Li, J.; Zhang, T. Heterogeneous Single-Atom Catalysis. *Nat. Rev. Chem.* **2018**, *2* (6), 65−81.

(13) Zhao, S.; Chen, G.; Zhou, G.; Yin, L. C.; Veder, J. P.; Johannessen, B.; Saunders, M.; Yang, S. Z.; De Marco, R.; Liu, C.; Jiang, S. P. A Universal Seeding Strategy to Synthesis Single Atom Catalysts on 2D Materials for Electrocatalytic Applications. *Adv. Funct. Mater.* **2020**, *30*, 1906157.

(14) Zhang, H.; Wei, J.; Dong, J.; Liu, G.; Shi, L.; An, P.; Zhao, G.; Kong, J.; Wang, X.; Meng, X.; Zhang, J.; Ye, J. Efficient Visible-Light-Driven Carbon Dioxide Reduction by a Single-Atom Implanted Metal-Organic Framework. *Angew. Chem., Int. Ed.* **2016**, *55* (46), 14310−14314.

(15) Wang, X.; Chen, Z.; Zhao, X.; Yao, T.; Chen, W.; You, R.; Zhao, C.; Wu, G.; Wang, J.; Huang, W.; Yang, J.; Hong, X.; Wei, S.; Wu, Y.; Li, Y. Regulation of Coordination Number over Single Co Sites: Triggering the Efficient Electroreduction of CO_2. *Angew. Chem., Int. Ed.* **2018**, *57* (7), 1944−1948.

(16) Ren, Y.; Tang, Y.; Zhang, L.; Liu, X.; Li, L.; Miao, S.; Sheng Su, D.; Wang, A.; Li, J.; Zhang, T. Unraveling the Coordination Structure-Performance Relationship in Pt_1/Fe_2O_3 Single-Atom Catalyst. *Nat. Commun.* **2019**, *10* (1), 4500.

(17) Zhou, P.; Chao, Y.; Lv, F.; Wang, K.; Zhang, W.; Zhou, J.; Chen, H.; Wang, L.; Li, Y.; Zhang, Q.; Gu, L.; Guo, S. Metal Single Atom Strategy Greatly Boosts Photocatalytic Methyl Activation and C-C Coupling for the Coproduction of High-Value-Added Multicarbon Compounds and Hydrogen. *ACS Catal.* **2020**, *10*, 9109−9114.

(18) Lee, S. H.; Choi, D. S.; Kuk, S. K.; Park, C. B. Photobiocatalysis: Activating Redox Enzymes by Direct or Indirect Transfer of Photoinduced Electrons. *Angew. Chem., Int. Ed.* **2018**, *57*, 7958.

(19) Huang, C.; Huang, Y.; Liu, C.; Yu, Y.; Zhang, B. Integrating Hydrogen Production with Aqueous Selective Semi-Dehydrogenation of Tetrahydroisoquinolines over a Ni_2P Bifunctional Electrode. *Angew. Chem., Int. Ed.* **2019**, *58* (35), 12014−12017.

(20) Hao, M.; Deng, X.; Xu, L.; Li, Z. Noble Metal Free MoS_2/$ZnIn_2S_4$ Nanocomposite for Acceptorless Photocatalytic Semi-Dehydrogenation of 1,2,3,4-Tetrahydroisoquinoline to Produce 3,4-Dihydroisoquinoline. *Appl. Catal., B* **2019**, *252*, 18−23.

(21) Zheng, M.; Shi, J.; Yuan, T.; Wang, X. Metal-Free Dehydrogenation of N-Heterocycles by Ternary h-BCN Nanosheets with Visible Light. *Angew. Chem., Int. Ed.* **2018**, *57* (19), 5487−5491.

(22) Tang, T.; Bi, X.; Meng, X.; Chen, G.; Gou, M.; Liu, X.; Zhao, P. MnO_x/Catechol/H_2O: A Cooperative Catalytic System for Aerobic Oxidative Dehydrogenation of N-Heterocycles at Room Temperature. *Tetrahedron Lett.* **2020**, *61* (5), 151425.

(23) Bi, X.; Tang, T.; Meng, X.; Gou, M.; Liu, X.; Zhao, P. Aerobic Oxidative Dehydrogenation of N-heterocycles over OMS-2-Based Nanocomposite Catalysts: Preparation, Characterization and Kinetic Study. *Catal. Sci. Technol.* **2020**, *10* (2), 360−371.

(24) Zhang, Y.; Zhao, Y.; Li, R.; Liu, J. Bioinspired NADH Regeneration Based on Conjugated Photocatalytic Systems. *Sol. RRL* **2020**, 2000339.

(25) Chen, Z.; Mitchell, S.; Vorobyeva, E.; Leary, R. K.; Hauert, R.; Furnival, T.; Ramasse, Q. M.; Thomas, J. M.; Midgley, P. A.; Dontsova, D.; Antonietti, M.; Pogodin, S.; López, N.; Pérez-Ramírez, J. Stabilization of Single Metal Atoms on Graphitic Carbon Nitride. *Adv. Funct. Mater.* **2017**, *27* (8), 1605785.
(26) Chen, Z.; Zhang, Q.; Chen, W.; Dong, J.; Yao, H.; Zhang, X.; Tong, X.; Wang, D.; Peng, Q.; Chen, C.; He, W.; Li, Y. Single-Site Au(I) Catalyst for Silane Oxidation with Water. *Adv. Mater.* **2018**, *30* (5), 1704720.
(27) Qin, Q.; Heil, T.; Antonietti, M.; Oschatz, M. Single-Site Gold Catalysts on Hierarchical N-Doped Porous Noble Carbon for Enhanced Electrochemical Reduction of Nitrogen. *Small Methods* **2018**, *2*, 1800202.
(28) Chen, Y.; Ji, S.; Wang, Y.; Dong, J.; Chen, W.; Li, Z.; Shen, R.; Zheng, L.; Zhuang, Z.; Wang, D.; Li, Y. Isolated Single Iron Atoms Anchored on N-Doped Porous Carbon as an Efficient Electrocatalyst for the Oxygen Reduction Reaction. *Angew. Chem., Int. Ed.* **2017**, *56*, 6937−6941.
(29) Wang, Y.; Zhao, X.; Cao, D.; Wang, Y.; Zhu, Y. Peroxymonosulfate Enhanced Visible Light Photocatalytic Degradation Bisphenol A by Single-Atom Dispersed Ag Mesoporous g-C_3N_4 Hybrid. *Appl. Catal., B* **2017**, *211*, 79−88.
(30) Liu, W.; Hu, W.; Yang, L.; Liu, J. Single Cobalt Atom Anchored on Carbon Nitride with Well-Defined Active Sites for Photo-Enzyme Catalysis. *Nano Energy* **2020**, *73*, 104750.
(31) Yan, C.; Li, H.; Ye, Y.; Wu, H.; Cai, F.; Si, R.; Xiao, J.; Miao, S.; Xie, S.; Yang, F.; Li, Y.; Wang, G.; Bao, X. Coordinatively Unsaturated Nickel−Nitrogen Sites Towards Selective and High-Rate CO_2 Electroreduction. *Energy Environ. Sci.* **2018**, *11* (5), 1204−1210.
(32) Chen, Z.; Vorobyeva, E.; Mitchell, S.; Fako, E.; López, N.; Collins, S. M.; Lear, R. K.; Midgley, P. A.; Hauert, R.; Pérez-Ramírez, J. Single-Atom Heterogeneous Catalysts Based on Distinct Carbon Nitride Scaffolds. *Natl. Sci. Rev.* **2018**, *5* (5), 642−652.
(33) Guan, J.; Duan, Z.; Zhang, F.; Kelly, S. D.; Si, R.; Dupuis, M.; Huang, Q.; Chen, J. Q.; Tang, C.; Li, C. Water Oxidation on a Mononuclear Manganese Heterogeneous Catalyst. *Nat. Catal.* **2018**, *1*, 870−877.
(34) Zhang, C.; Sha, J.; Fei, H.; Liu, M.; Yazdi, S.; Zhang, J.; Zhong, Q.; Zou, X.; Zhao, N.; Yu, H.; Jiang, Z.; Ringe, E.; Yakobson, B. I.; Dong, J.; Chen, D.; Tour, J. M. Single-Atomic Ruthenium Catalytic Sites on Nitrogen-Doped Graphene for Oxygen Reduction Reaction in Acidic Medium. *ACS Nano* **2017**, *11* (7), 6930−6941.
(35) He, L.; Weniger, F.; Neumann, H.; Beller, M. Synthesis, Characterization, and Application of Metal Nanoparticles Supported on Nitrogen-Doped Carbon: Catalysis beyond Electrochemistry. *Angew. Chem., Int. Ed.* **2016**, *55* (41), 12582−94.
(36) Wu, Y.; Chen, Z.; Cheong, W.-C.; Zhang, C.; Zheng, L.; Yan, W.; Yu, R.; Chen, C.; Li, Y. Nitrogen-Coordinated Cobalt Nanocrystals for Oxidative Dehydrogenation and Hydrogenation of N-heterocycles. *Chem. Sci.* **2019**, *10*, 5345−5352.
(37) Liu, P. X.; Zhao, Y.; Qin, R. X.; Mo, S. G.; Chen, G. X.; Gu, L.; C, D. M.; Zhang, P.; Guo, Q.; Zang, D. D.; Wu, B. H.; Fu, G.; Zheng, N. F. Photochemical Route for Synthesizing Atomically Dispersed Palladium Catalysts. *Science* **2016**, *352* (6287), 797−800.
(38) Cai, J.; Huang, J.; Wang, S.; Iocozzia, J.; Sun, Z.; Sun, J.; Yang, Y.; Lai, Y.; Lin, Z. Crafting Mussel-Inspired Metal Nanoparticle-Decorated Ultrathin Graphitic Carbon Nitride for the Degradation of Chemical Pollutants and Production of Chemical Resources. *Adv. Mater.* **2019**, *31* (15), 1806314.
(39) Hu, Y.; Huang, W.; Wang, H.; He, Q.; Zhou, Y.; Yang, P.; Li, Y.; Li, Y. Metal-Free Photocatalytic Hydrogenation Using Covalent Triazine Polymers. *Angew. Chem., Int. Ed.* **2020**, *59* (34), 14378−14382.
(40) Liu, J.; Antonietti, M. Bio-Inspired NADH Regeneration by Carbon Nitride Photocatalysis Using Diatom Templates. *Energy Environ. Sci.* **2013**, *6* (5), 1486−1493.
(41) Reyes, R. L.; Sato, M.; Iwai, T.; Suzuki, K.; Maeda, S.; Sawamura, M. Asymmetric Remote C-H Borylation of Aliphatic Amides and Esters with a Modular Iridium Catalyst. *Science* **2020**, *369* (6506), 970−974.
(42) Feng, G.; Cheng, P.; Yan, W.; Boronat, M.; Li, X.; Su, J.-H.; Wang, J.; Li, Y.; Corma, A.; Xu, R.; Yu, J. Accelerated Crystallization of Zeolites via Hydroxyl Free Radicals. *Science* **2016**, *351* (6278), 1188−1191.
(43) An, S.; Zhang, G.; Wang, T.; Zhang, W.; Li, K.; Song, C.; Miller, J. T.; Miao, S.; Wang, J.; Guo, X. High-Density Ultra-Small Clusters and Single-Atom Fe Sites Embedded in Graphitic Carbon Nitride (g-C_3N_4) for Highly Efficient Catalytic Advanced Oxidation Processes. *ACS Nano* **2018**, *12* (9), 9441−9450.
(44) Li, J.; Chen, Y.; Yang, X.; Gao, S.; Cao, R. Visible-Light-Mediated High-efficiency Catalytic Oxidation of Sulfides Using Wrinkled C_3N_4 Nanosheets. *J. Catal.* **2020**, *381*, 579−589.

https://dx.doi.org/10.1021/acscatal.0c04651
ACS Catal. 2021, 11, 313−322